ACS APPLIED MATERIALS & INTERFACES

Research Article

www.acsami.org

Envelopment–Internalization Synergistic Effects and Metabolic Mechanisms of Graphene Oxide on Single-Cell *Chlorella vulgaris* Are Dependent on the Nanomaterial Particle Size

Shaohu Ouyang, Xiangang Hu,* and Qixing Zhou*

†Key Laboratory of Pollution Processes and Environmental Criteria (Ministry of Education)/Tianjin Key Laboratory of Environmental Remediation and Pollution Control, College of Environmental Science and Engineering, Nankai University, Tianjin 300071, China

Supporting Information

ABSTRACT: The interactions between nanomaterials and cells are fundamental in biological responses to nanomaterials. However, the size-dependent synergistic effects of envelopment and internalization as well as the metabolic mechanisms of nanomaterials have remained unknown. The nanomaterials tested here were larger graphene oxide nanosheets (GONS) and small graphene oxide quantum dots (GOQD). GONS intensively entrapped single-celled *Chlorella vulgaris*, and envelopment by GONS reduced the cell permeability. In contrast, GOQD-induced remarkable shrinkage of the plasma membrane and then enhanced cell permeability through strong internalization effects such as plasmolysis, uptake of nanomaterials, an oxidative stress increase, and inhibition of cell division and chlorophyll biosynthesis. Metabolomics analysis showed that amino acid metabolism was sensitive to nanomaterial exposure. Shrinkage of the plasma membrane is proposed to be linked to increases in the isoleucine levels. The inhibition of cell division and chlorophyll a biosynthesis was associated with decreases in aspartic acid and serine, the precursors of chlorophyll a. The increases in mitochondrial membrane potential loss and oxidative stress were correlated with an increase in linolenic acid. The above metabolites can be used as indicators of the corresponding biological responses. These results enhance our systemic understanding of the size-dependent biological effects of nanomaterials.

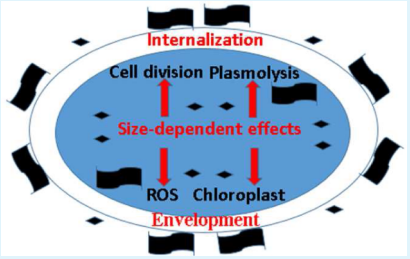

KEYWORDS: *graphene oxide, quantum dot, nanotoxicology, single cell, reactive oxygen species, metabolomics*

INTRODUCTION

Graphene oxide (GO), a novel engineered nanomaterial with a thickness of approximately 1 nm, has been applied in various fields, including chemistry, medicine, biology, and environmental protection.[1,2] Compared with other nanomaterials, GO exhibits excellent mechanical and hydrophilic properties while remaining highly flexible and ductile.[3] The flexible and ductile properties facilitate the adherence of GO to cellular surfaces.[4] Therefore, the interactions of GO with cells have received much interest from researchers studying the biological effects of nanomaterials.[5] In the potential interactions between graphene-related materials and cells, envelopment and internalization are the fundamental interactional patterns, and these processes typically occur simultaneously.[5] The effects of internalization, such as clathrin-mediated endocytosis, lysosomal or other perinuclear compartment localization, and oxidative stress, have been well studied, but the effects of nanomaterial envelopment (biological responses after nanomaterial adhesion onto the outer surface of the cell wall or membrane) remain unknown.[6,7]

Some studies have suggested that when GO is incubated with cells, it forms a cell-assembled graphene biocoating for enhanced chondrogenic differentiation, even protecting against cell swelling, leakage, enzymatic attachment, and UV irradiation.[7,8] Viability tests have also indicated that GO encapsulation was compatible with living cells.[9,10] In contrast, other studies have demonstrated that small hydrophobic graphene sheets pierced through the phospholipid membrane and navigated the double layer and that the envelopment of embryos by GO-induced hypoxia promoted oxidative stress and caused biological malformation.[11,12] In addition, the internalization effects of graphene-related materials should also be considered. Endocytosis and passive diffusion are general entry mechanisms for various extracellular materials.[13] Because of the challenge of accurately quantifying GO, the cellular uptake paths dependent on the nanomaterial size and the cell wall barrier and the specific cellular responses to nanomaterial envelopment or internalization remain obscure. Herein, the synergistic effects of GO envelopment and internalization were considered to address the relevant questions.

The nanomaterial size plays a major role in the biocompatibility of these materials. The nanomaterial size significantly affected multiple cellular parameters (i.e., cellular viability, oxidative stress, and cellular activation).[14−17] Several studies have reported that the in vitro cytotoxicity and

Received: June 15, 2015
Accepted: July 29, 2015
Published: July 29, 2015

DOI: 10.1021/acsami.5b05328
ACS Appl. Mater. Interfaces 2015, 7, 18104−18112

intracellular uptake mechanisms of nanoparticles are dependent on the size and/or aggregation state of these materials; for example, dispersed and small-sized graphene molecules were more toxic than their aggregated counterparts.[14−17] Compared with a larger GO nanosheet (GONS), GO quantum dots (GOQD) assume the same motif as a conventional GONS, with a lateral dimension of less than 100 nm and fluorescent characteristics that contribute to the wide application of this material.[18,19] Until recently, the biological effects of GOQD were unknown. Herein, we performed a comparable exploration of the envelopment−internalization synergistic effects of GONS (lateral length, 1−5 μm) and GOQD (lateral length, approximately 20−50 nm).

The selection of toxicological end points also influences the experimental conclusions. Cell viability, cell division, cell ultrastructure, and oxidative stress are the common toxicological end points of nanomaterials.[20] Metabolites serve as direct signatures of biochemical activities and are easy to correlate with cellular biochemistry and biological phenomena.[21] For evaluation of the nanomaterial safety, the potential unique benefits of applying metabolomics, particularly single-cell metabolomics, have only recently been recognized.[22,23] In the present study, the multiple toxicological end points (cell division, cell ultrastructure, oxidative stress, and cell metabolism) of the single-celled organism *Chlorella vulgaris* were employed to explore the specific effects of GONS and GOQD.

MATERIALS AND METHODS

Characterization of Nanomaterials Provided in the Supporting Information. *Cell Division.* *C. vulgaris* was purchased from the Institute of Wuhan Hydrobiology, Chinese Academy of Sciences. The algal cells were cultured in 250 mL glass flasks containing 100 mL of a BG-11 medium (Table S1) in the presence or absence of different concentrations (0.01, 0.1, 1.0, and 10.0 mg/L) of GONS and GOQD. The glass flasks containing algae were placed in an illumination incubator (LRH-250 Gb, China) at 24.0 ± 0.5 °C and 80% humidity. The inhibition of cell division was calculated daily using CASY TT (Innovatis, Germany). The initial density of algal cells was approximately 6.5×10^4 cells/mL. The cell division inhibition rates (%) were identified as the cell numbers in nanomaterial exposure groups subtracted from the cell numbers in the control and then divided by the cell numbers in the control. The proportions of dead cells were detected by flow cytometric analysis with propidium iodide staining. Cell suspension was centrifuged at 9000*g* for 5 min, washed using phosphate-buffered saline (PBS), and then stained with propidium iodide for 20 min. The fluorescent intensity was analyzed on a flow cytometry (CyFLOW Space, Partec, Germany). To measure chlorophyll a, 4 mL of the algal cell suspension was centrifuged at 9000*g* for 5 min. Subsequently, 4 mL of 95% ethanol was added to the suspended cells and incubated in the dark for 24 h. The chlorophyll a content in 95% ethanol was measured at 665 and 649 nm using a UV−vis spectrophotometer (TU-1900, Persee, China).

Cell Permeability. Cell permeability was determined using the fluorescein diacetate (FDA) method. FDA is a nonpolar, hydrophobic, and nonfluorescent esterified compound that freely enters cells. The algal cell suspension (1 mL) was centrifuged (9000*g*, 5 min) and washed three times with a fresh BG-11 medium, and then FDA was added at a final concentration of 10 μg/mL. The suspension was then incubated for 30 min under dark conditions at room temperature, centrifuged (12000*g*, 2 min), and washed three times with PBS. The fluorescent samples were examined using a fluorescence microscope (LS55, PerkinElmer, USA) with excitation at 485 nm and emission at 521 nm. The results are shown as the fluorescence intensity per 10^6 cells.

Fourier Transform Infrared (FTIR). FTIR spectroscopy was used to identify the functional groups and structures on the surface of the cells. The algal cells were harvested through centrifugation at 9000*g* at 25 °C for 5 min and washed three times with PBS. Subsequently, the cells were filtered through a 0.2 μm poly(tetrafluoroethylene) membrane and then freeze-dried. A Bruker Tensor 27 FTIR spectrometer was used to record the IR spectra, and the spectra from 1000 to 3500 cm^{-1} were collected with a resolution of 2 cm^{-1}.

Electron Microscopy Observation. Envelopment of algal cells by nanomaterials was observed using scanning electron microscopy (SEM; SU8010, Hitachi, Japan). Algal suspensions of 5 mL were obtained through centrifugation (9000*g*, 5 min), chemically fixed for 2 h using 2.5% glutaraldehyde, washed three times with PBS, and subsequently postfixed in 1% osmium tetroxide for 2 h. Subsequently, the samples were dehydrated in a graded ethanol series (30%, 50%, 70%, 80%, 90%, 95%, and 100%) for 10 min each, washed with *tert*-butyl alcohol, and air-dried under vacuum. The cellular ultrastructure was observed through transmission electron microscopy (TEM; HT7700, Hitachi, Japan). The cells were collected after centrifugation of the 5 mL suspension. After washing with PBS, the cells were fixed in 2.5% glutaraldehyde overnight at 4 °C, postfixed in 1% osmium tetroxide for 2 h, dehydrated in a graded ethanol series (30%, 50%, 70%, 80%, 90%, 95%, and 100%), and then embedded in an epoxy resin. Ultrathin sections (90 nm) of algal cells were cut with a diamond knife (EM FC7, Leica, Germany) on an ultramicrotome and stained with uranyl acetate and lead citrate for 15 min.

Nanomaterial Internalization. To prepare the calibration curve for the quantification of nanomaterial internalization, 20 mL of the algal suspension cultured for 96 h without nanomaterial exposure was collected after centrifugation (9000*g*, 5 min) and suspended using 3 mL of a BG-11 medium. Nanomaterials (0.02, 0.2, 2.0, and 20.0 μg) were spiked into the above algal suspension, and the algal cells were substantially broken using an ultrasonic cell disruptor in an ice bath. The cells were exposed to the sonication probe tip at 150 W for 15 min to ensure that the nanomaterials were homogeneously distributed in the cell matrix. The cell matrix containing nanomaterials was lyophilized and then placed on microscope slides. The quantification of nanomaterial internalization was performed by confocal Raman spectroscopy (RS; Thermo Scientific, DXR, USA) at 780 nm, and the intensity of the G bands was recorded. The nanomaterials in the exposed groups were quantified using the procedure described above.

Reactive Oxygen Species (ROS) and Superoxide Dismutase (SOD) Assay. 2′,7′-Dichlorodihydrofluorescein diacetate (DCFH-DA) was used to measure intracellular ROS. DCFH-DA entered the algal cells, reacted with ROS, and then produced the highly fluorescent compound dichlorofluorescein (DCF). Briefly, 1 mL of the algal suspension was collected after centrifugation (9000*g*, 5 min) and then washed three times with PBS. The algal cells were incubated with DCFH-DA (10 μM) in the dark at 25 °C for 30 min. The algal cells were then washed an additional three times with PBS. The fluorescence intensity of DCF was measured using a fluorescence spectrophotometer (LS55, PerkinElmer, USA) with an excitation wavelength of 485 nm and an emission wavelength of 530 nm. The SOD activity was spectrophotometrically determined using a SOD assay kit (A001-2, Nanjing JianCheng Bioengineering Institute, Nanjing, China) according to the manufacturer's instructions. The absorbance was read at 450 nm using a UV−vis spectrophotometer (TU-1900, Persee, China). Relative SOD levels were calculated as the ratios of the treatments to the control.

Mitochondrial Membrane Potential Loss. For this assay, 1 mL of an algal suspension was collected after centrifugation (9000*g*, 5 min), washed three times with PBS, and then incubated with 10 mM 5,5′,6,6′-tetrachloro-1,1′,3,3′-tetraethylbenzimidazolylcarbocyanine iodide (JC-1) for 1 h in the dark at 37 °C. Before the observation, algae were washed again with PBS. The JC-1-stained algal cells were observed by fluorescence microscopy (IX71, Olympus, Japan) with a 475 nm excitation wavelength, and the corresponding fluorescence intensities were collected at 530 nm (green) and 590 nm (red). Images were acquired using the *Photoshop 7.0* software package. Images and fluorescence intensities were analyzed using *ImageJ* software. Measurement of the mitochondrial membrane potential loss was recorded as the ratios of red-to-green emission intensities (I590/I530).

DOI: 10.1021/acsami.5b05328
ACS Appl. Mater. Interfaces 2015, 7, 18104−18112

Metabolic Analyses. The cells were collected from 10 mL of the algal suspension after centrifugation (9000*g*, 5 min). To avoid metabolic alterations during the preparation and to completely break the cell walls, collection was followed by three cycles of freezing in liquid nitrogen and thawing. Subsequently, a 4.5 mL solution of methanol/chloroform/water (volumetric ratio = 2.5:1:1) was spiked into the cell suspension, and the cells were completely broken using an ultrasonic cell disruptor (150 W, 10 min) in an ice bath. The metabolites were extracted using ultrasound (200 W, 30 min), followed by centrifugation for 5 min at 9000*g* at 4 °C. The supernatant was collected, and after ultrasound and centrifugation as described above, the sediment was extracted again using 4.5 mL of a methanol/chloroform/water solution (volumetric ratio = 2.5:1:1). The supernatant was mixed with the previously collected supernatant. Water (1.5 mL) was added into the above supernatant and then centrifuged at 9000*g* for 5 min. The lower phase was filtered through a 5 cm silica gel column and dried via nitrogen blow-off. For the upper phase, methanol and water were removed via nitrogen blow-off and lyophilization, respectively, and subsequently mixed with the residual lower-layer phase. Methoxamine hydrochloride (20 mg/mL, 50 μL) and *N*-methyl-*N*-(trimethylsilyl)trifluoroacetamide (80 μL) were added as derivatives. The samples (1 μL) were injected into the gas chromatography column in split mode (1:25). Metabolic analyses were conducted using gas chromatography with quadruple mass spectrometry (GC−MS; 6890N/5973, Agilent, USA).

Statistical Analysis. All of the experiments were performed in triplicate, and the results are presented as the mean ± standard deviation. One-way analysis of variance (ANOVA) using least significant difference followed by Duncan's test was employed to analyze the statistical significance of the exposed groups compared with the control. Statistical significance "*" was accepted at a level of $p < 0.05$.

RESULTS

Nanomaterial Characterization. The TEM images of GONS and GOQD in Figure 1a,b show irregular folds on GONS, reflecting the flexibility of GONS. Parts c and d of Figure 1 show the atomic force microscopy (AFM) images of the nanomaterials. The thicknesses of GONS and GOQD were approximately 0.8−1.0 and 4.8−5.2 nm, respectively. The AFM and TEM images also showed that the lateral lengths of GONS and GOQD were approximately 1−5 μm and 20−50 nm, respectively. Furthermore, the material dispersity was investigated, as shown in Figure 2a, and the ζ potential became negative with increasing pH, suggesting that the surfaces of both materials exhibited negative charges at pH 7−11. GOQD exhibited more negative charges than GONS at pH 7−11, suggesting that GOQD has a better dispersity than GONS because of electrostatic repulsion (the pH of the cell culture medium was 7.4). The free electrons of nanomaterials were examined through electron paramagnetic resonance (EPR), as shown in Figure 2b. The peak shapes and intensities of GONS and GOQD were comparable. X-ray photoelectron resonance (XPS) was conducted to describe the surface chemistry of GONS and GOQD. As shown in Figure 2c, GONS includes 67.17% C 1s, 30.37% O 1s, and 2.47% S 2p. Figure 2d shows that GOQD contains 78.2% C 1s, 16.5% O 1s, and 5.3% Na 1s. The limited elements sulfur and sodium were the agents involved in chemical synthesis.

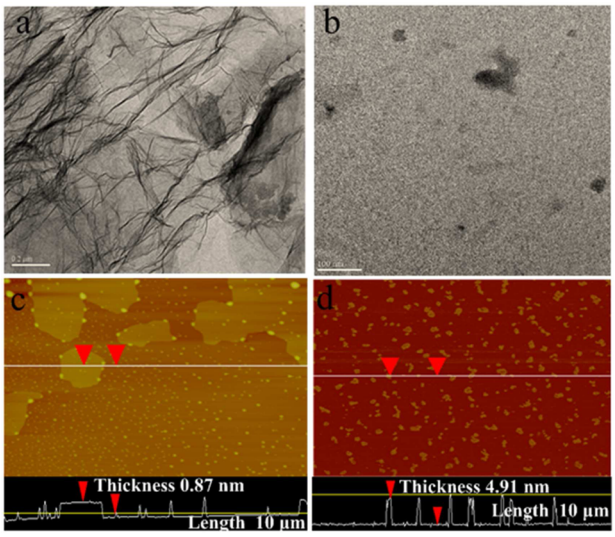

Figure 1. Nanomaterial morphology: (a) field-emission TEM image of GONS; (b) field-emission TEM image of GOQD; (c) AFM image of GONS; (d) AFM image of GOQD. Scale bars: (a) 0.2 μm; (b) 0.1 μm; (c) image lateral length of 10 μm; (d) image lateral length of 10 μm.

Envelopment of Cells through Nanomaterials. SEM images were obtained to explore the envelopment of algal cells through GONS and GOQD, as shown in Figure 3a−c. The diameters of the cells were similar in all groups and were approximately 5 μm. In control cells, irregular ruffles forming grooves of approximately 0.5 μm diameter covered the surface of the cells. However, as shown in Figure 1b,c, the ruffles were not obvious for cells exposed to GONS and GOQD, and an unknown compound filled the grooves on the surface of cells, as denoted by the red arrows. To determine the chemical composition of the unknown compound described above, RS was performed as shown in Figure 3d. For cells exposed to GONS, the typical D and G bands were clearly detected, suggesting that GONS covered the surfaces of the cells. For cells exposed to GOQD, the D and G bands were not significant. The red shift in the RS peaks for GOQD might reflect interactions with the intercellular environment.[24] In addition, RS also showed that, compared with control conditions, cell secretion decreased when the cells were covered by GONS but not when they were covered by GOQD, indicated by the blue arrow. This may be explained by the finding that GONS envelops the cells and that GOQD does not, as shown in Figure 3b,c. The RS of cells enveloped by GONS reflects strong signals of GONS rather than the natural cell surface, as shown by the D and G peaks in Figure 3b.

Alterations of the Cell Surface Chemistry. FTIR was performed to identify alterations in the cell surface chemistry after envelopment by nanomaterials. As described in Figure 4, the absorbance of CO_2 from the atmosphere is obvious in GONS using two-dimensional sheet morphology, and the CO_2 peak remained significant after GONS were immobilized onto algal cells. In the GOQD condition, a CO_2 peak did not appear, but on the surfaces of cells exposed to GOQD, the CO_2 peak, denoted by the green arrow, was obvious, likely because of cell respiration. After entrapment by nanomaterials, the O−H/N−H/C−H/C = N/N−N peaks increased, as indicated by black and pink arrows. Compared with GONS, GOQD enhanced the peaks of C−O/N−O/C−N/N−H, as indicated by blue and red arrows. Considering that the above groups were not detected in GONS/GOQD samples or on pristine cell surfaces, the increases in those chemical groups presumably result from alterations in the cell walls after nanomaterial envelopment.

Alterations of the Cell Permeability. Alterations of the cell permeability after envelopment of nanomaterials were explored, as shown in Figure 5a. There was no significant

DOI: 10.1021/acsami.5b05328
ACS Appl. Mater. Interfaces 2015, 7, 18104−18112

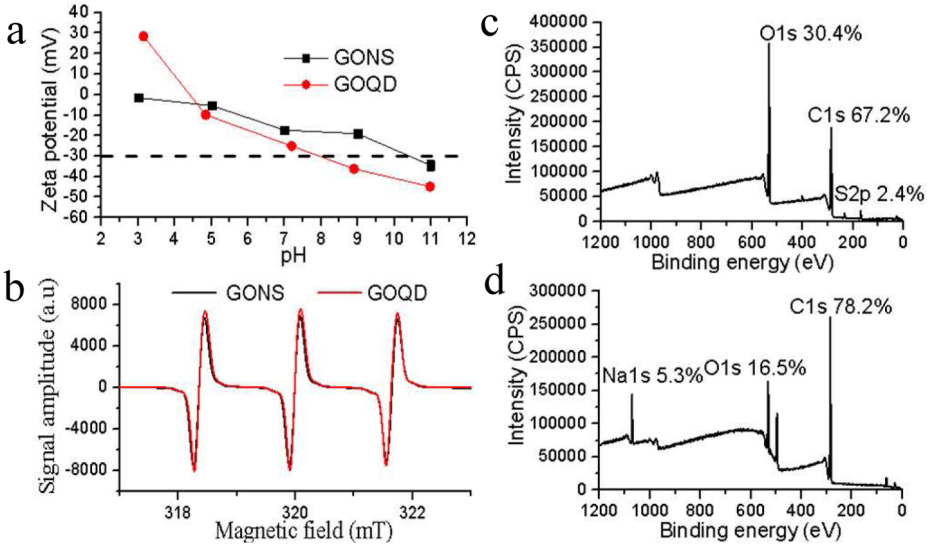

Figure 2. Chemical properties of nanomaterials: (a) ζ potential; (b) EPR spectra; (c) XPS spectrum of GONS; (d) XPS spectrum of GOQD.

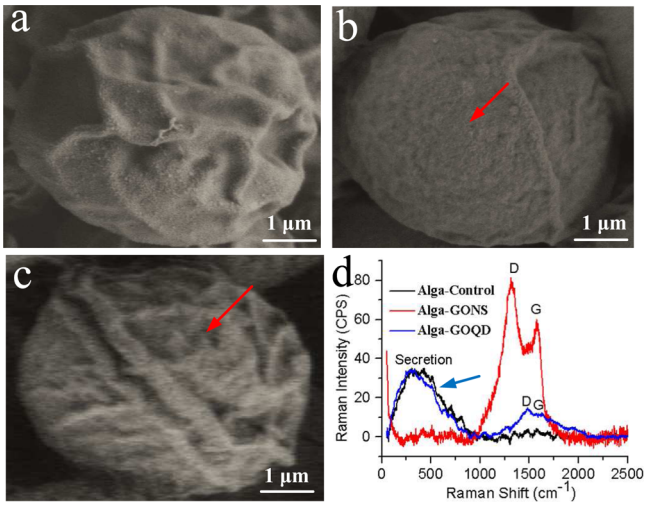

Figure 3. Envelopment of the cells by nanomaterials at 96 h. SEM images of the cells in the (a) absence and presence of 10.0 mg/L GONS (b) and 10.0 mg/L GOQD (c). The red arrows denote the envelopment phenomena of the nanomaterials. Furthermore, RS spectra (d) were conducted to determine the chemical composition of the envelopment coating SEM images. The blue arrow denotes algal secretion.

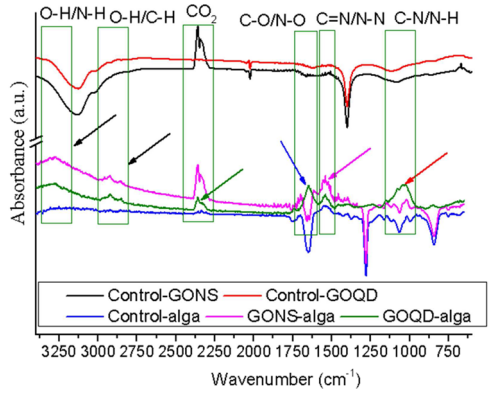

Figure 4. FTIR spectra of the controls (GONS power, GOQD power, and cell surface without nanomaterial exposure) and the cell surface exposed to nanomaterials. The arrows denote alterations in the chemical groups.

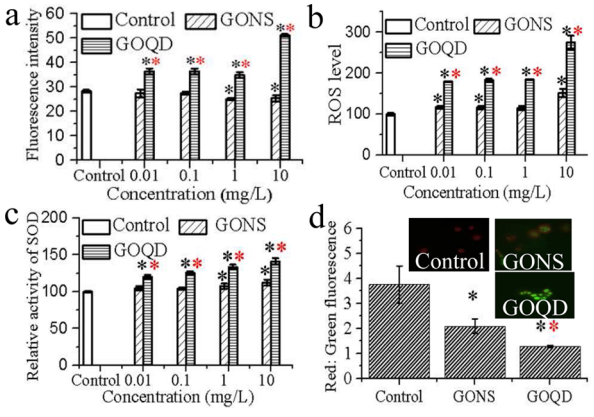

Figure 5. Alterations in the cell permeability (a), intracellular ROS levels, (b) SOD activities, (c) and mitochondrial membrane potential loss (d) after exposure to nanomaterials for 96 h. The mitochondrial membrane potential loss in algal cells exposed to 0 mg/L nanomaterials is shown via JC-1 staining. Black and red "*" denote significant differences compared to the control and GONS groups, respectively, at $p < 0.05$.

difference between the control and the cells exposed to GONS, except for the high-concentration exposure at 1 and 10 mg/L. At 0.01 and 1 mg/L GONS exposure, there were no significant alterations in the fluorescence intensity compared with the control. In contrast, the fluorescence intensity significantly increased by 12.6%, 30.0%, 24.3%, and 82.5% with 0.01, 0.1, 1, and 10 mg/L GOQD, respectively. Unlike the traditional views that the cell permeability only reflects damage to the cell wall/plasma membrane, these results suggest that envelopment of nanomaterials also directly influences the cell permeability, specifically by decreasing the cell permeability.

Intracellular Oxidative Stress. As shown in Figure 5b, both GONS and GOQD at 0.01−10 mg/L significantly promoted the production of ROS. The relative ROS levels in the GONS and GOQD groups were 10.5−52.1% and 79.6−175.4% higher than the control, respectively. The ROS level in

DOI: 10.1021/acsami.5b05328
ACS Appl. Mater. Interfaces 2015, 7, 18104−18112

the GOQD group was significantly higher than that in the GONS group. Furthermore, the activities of SOD confirm changes in the oxidative stress, as shown in Figure 5c. High concentrations of GONS, 1 and 10 mg/L, induced upregulation of the SOD activity, while at concentrations ranging from 0.01 to 10 mg/L, GOQD induced upregulation of the SOD activity. GOQD induced stronger upregulation of the SOD activity than GONS. The mitochondrial membrane potential loss associated with intracellular oxidative stress was evaluated by JC-1 staining. As shown in Figure 5d, the ratios of red-to-green fluorescence intensity significantly decreased by 44.40% ($p < 0.01$) and 66.09% ($p < 0.01$) after exposure to 10.0 mg/L GONS and GOQD, respectively, compared with the control. This result suggests that GOQD induces stronger oxidative stress than GONS.

Alterations of the Cellular Ultrastructure. As shown in Figure 6, TEM was performed to observe alterations in the cellular ultrastructure. Figure 6a shows TEM images of control cells with intact cell walls, plasma membranes, and chloroplastic, nuclear, and other cytoplasmic compartments. However, GONS and GOQD induce significant plasmolysis, as indicated by the double black arrows in parts b and c of Figure 6, respectively. Analysis of TEM images showed that the ratios of the plasmolysis area to total cell area were 17.1% and 13.8% after GONS and GOQD exposure, respectively, and these parameters were significantly higher than those in the control (9%). Compared with the typical shape of the cell wall in all groups, shrinkage of the plasma membrane led to plasmolysis. Shrinkage of the plasma membrane after GONS exposure was more obvious than that after GOQD exposure. In addition, the structures of the chloroplasts and thylakoids were indistinct in cells exposed to nanomaterials. GOQD significantly induces the downregulation of chlorophyll a biosynthesis, as shown in Figure S1. The numbers of starch grains and lysosomes significantly increased after nanomaterial exposure, as shown in Figure 6b,c. The numbers of starch grains after GONS and GOQD exposure were 2.6- and 4.0-fold larger than that in the control, respectively, as shown in Figure 6d. The numbers of lysosomes after GONS and GOQD exposure were 2.0- and 3.7-fold larger than that in the control, respectively.

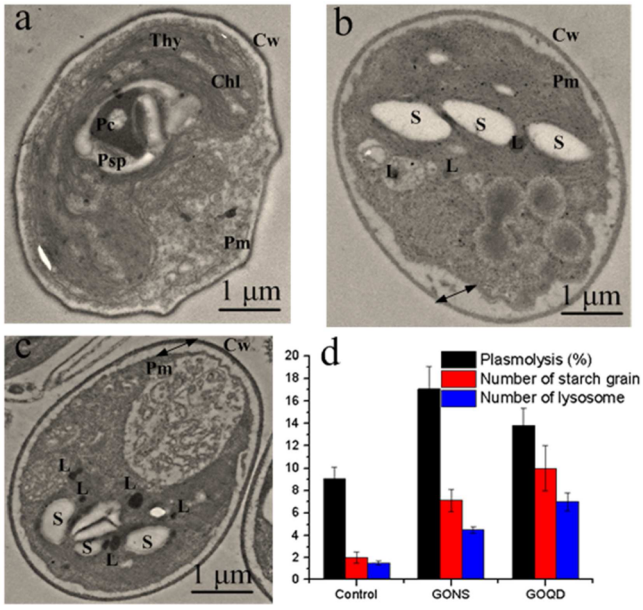

Figure 6. TEM images of cells: (a) control without nanomaterial exposure; (b) 10 mg/L GONS exposure; (c) 10 mg/L GOQD exposure; (d) statistical analysis of TEM images ($n > 15$). The double black arrows denote plasmolysis. Abbreviations: Cw, cell wall; Pm, plasma membrane; L, lysosome; S, starch grain; Chl, chloroplast; Thy, thylakoids; Pc, pyrenoid center; Psp, pyrenoid starch plate.

Cellular Internalization of Nanomaterials. RS was used to determine the uptake of GONS and GOQD in algal cells. GONS and GOQD were spiked into the algal matrix to prepare calibration curves with linear correlation coefficients higher than 0.9. The uptake rates were identified as the ratios of the nanomaterial mass in cells to the cell mass. The uptake percentages were defined as the ratios of the nanomaterial mass in cells to the total nanomaterial mass in the cell suspension. The uptake rates of GONS at 0.01, 0.1, and 1 mg/L were 0.4, 2.7, and 23.3 μg/g, respectively. The uptake percentages of GONS at 0.01, 0.1, and 1 mg/L were 1.2%, 0.7%, and 0.7%, respectively. The uptake rates of GOQD at 0.01, 0.1, and 1 mg/L were 4.7, 439, and 913 μg/g, respectively. The uptake percentages of GOQD at 0.01, 0.1, and 1 mg/L were 13.7%, 61.5%, and 27.4%, respectively. These data suggest that the cellular internalization levels of GOQD are approximately 10–80-fold higher than those of GONS.

Cell Division. Figure 7 shows the envelopment–internalization effects of nanomaterials upon cell division. The initial number of cells was 6.5×10^4 cells/mL. At 24 h, cell division was promoted by increasing the concentrations of nanomaterials. The cell numbers after GONS and GOQD exposure were 12.1–90.5% and 53.7–76.5% higher than those in the control, respectively. At 48 h, the cell numbers after GONS and GOQD exposure were 5.7–64.9% and 16.6–55.9% higher than those in the control, respectively. However, at 72 h, cell division was promoted by GONS but inhibited by GOQD. At 96 h, both nanomaterials inhibited cell division. The cell numbers after GONS and GOQD exposure decreased 1.9–15.9% and 20.1–46.8%, respectively, compared with the control. These results showed that GONS and GOQD first promoted and then inhibited algal cell division. Moreover, GOQD led to a more

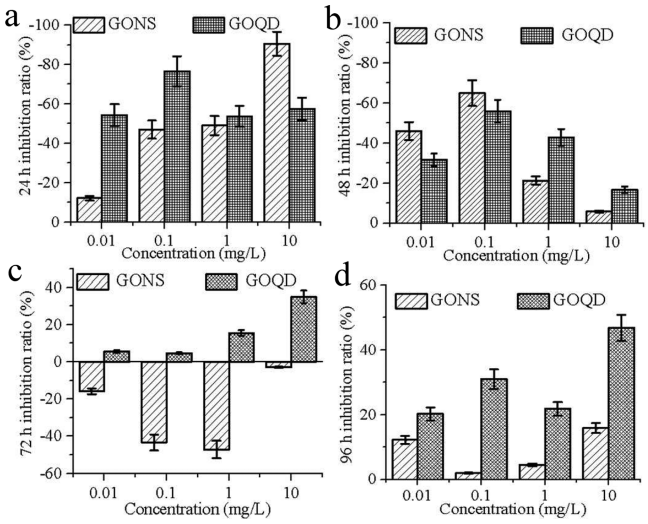

Figure 7. Cell division under nanomaterial exposure at (a) 24, (b) 48, (c) 72, and (d) 96 h. The inhibition ratios are defined as the cell numbers in nanomaterial exposure groups subtracted from the cell numbers in the control and then divided by the cell numbers in the control.

DOI: 10.1021/acsami.5b05328
ACS Appl. Mater. Interfaces 2015, 7, 18104–18112

marked inhibition of cell division than GONS. The proportions of dead cells were also detected, as shown in Table S2. Neither GONS nor GOQD remarkably induced the death of cells, and the proportions of dead cells were less than 3% in all tested groups.

Metabolic Analysis. Approximately 160−190 peaks in each sample were analyzed using GC−MS with derivatization preparation, and 36 metabolites were identified, as shown in Tables S3 and S4. The 36 identified metabolites include amino acids, carbohydrates, fatty acids, tricarboxylic acid, and other small molecular metabolites. The metabolite levels in the control and nanomaterial-exposed groups are presented using thermal maps. Figure 8a shows the relative levels of the 36

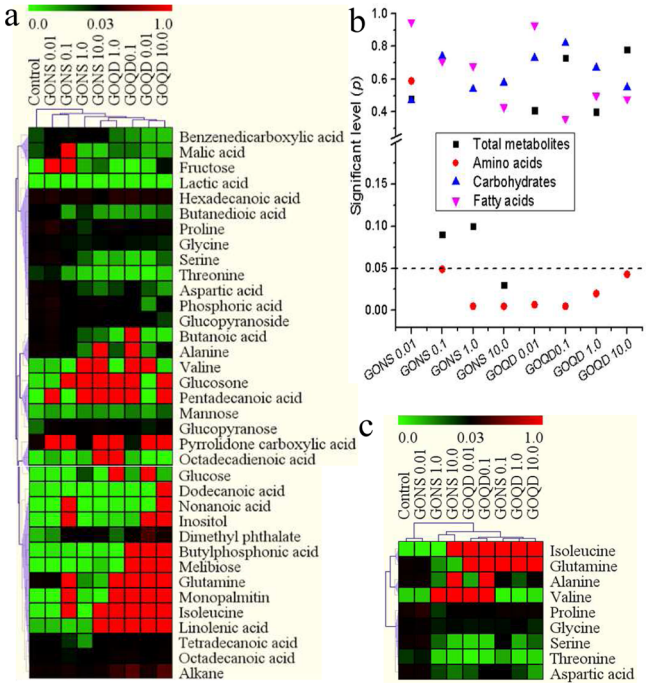

Figure 8. Thermal map reflecting the metabolic levels in the control and nanomaterial exposure groups: (a) thermal map of all identified metabolites; (b) significant differences in the levels of exposure groups compared with the control; (c) thermal maps of amino acids. Cluster analysis of the metabolites was conducted using an HCL model.

metabolites identified. These metabolites were divided into two groups by hierarchical clustering (HCL) analysis: control and exposure groups. Moreover, the exposure groups were divided into GONS 0.01/GONS 0.1 and other exposure groups. HCL analysis demonstrated that nanomaterials induced alterations in metabolism. Furthermore, several metabolites (amino acids, carbohydrates, and fatty acids) were individually analyzed to explore the significant differences in exposure groups compared with the control, as shown in Figure 8b. For a combination of the 36 metabolites identified, no significant differences from the control were observed among exposure groups except for GONS at 10 mg/L. For carbohydrate and fatty acid metabolism, no significant differences in the exposure groups were observed compared with the control. However, for amino acid metabolism, significant differences from the control were observed for all exposure groups except for GONS at low concentrations of 0.01 and 0.1 mg/L. The above analysis implies that amino acid metabolism is sensitive to exposure to nanomaterials. The relative metabolism levels of individual amino acids were further analyzed, as shown in Figure 8c. Metabolites were divided into two groups: control/GONS 0.01 and other exposure groups. Compared with the control, nanomaterial exposure induced increases in the isoleucine and glutamine levels, particularly after GOQD exposure. In contrast, the levels of serine and threonine were downregulated after nanomaterial exposure at the high concentrations of 1 and 10 mg/L.

DISCUSSION

Figure 3 shows that GONS obviously entraps cells. Until recently, the entrapment mechanism was unclear. In Figure 1, the AFM and TEM images show that GONS presented a flexible nanosheet morphology. This characteristic facilitated the adhesion of GONS onto cells. The oxygen- and hydrogen-containing groups on nanomaterials could also drive the adhesion of nanomaterials onto cell surfaces through hydrophobic, receptor−ligand, and hydrogen-binding interactions.[2,25] In Figure 2, the ζ potential shows that the nanomaterial surface was negatively charged at pH 6−11. Given the negative charges on algal cells,[26] electrostatic interactions did not contribute to the wrapping of cells with nanomaterials. The cellular adhesion onto GONS was stronger than that onto graphene,[27] suggesting that, in the interactions of GONS with cells, hydrogen bonding from hydrogen- and oxygen-containing groups played a more important role than $\pi-\pi$ stacking from sp^2 structures. This hypothesis was supported by the results of the FTIR spectra shown in Figure 4.

The reduction of the cell permeability after GONS exposure confirmed the envelopment of GONS. This result was consistent with the cytoprotective roles of GONS, for instance, the inhibition of cell leakage.[7,28] Maheshwari et al. also demonstrated the protection of *Saccharomyces cerevisiae* against osmotic pressure after coating the cells with reduced GONS.[29] In contrast, GOQD enhanced the cell permeability. Given that TEM images show that GONS induced stronger plasma membrane shrinkage than did GOQD, the envelopment effects might play a dominant role in the reduction of the cell permeability. There was no significant breakage in the cell wall when nanomaterials were detected on the surfaces of the cells. The TEM results were consistent with Raman mapping, showing that GONS and GOQD were located in the cytoplasm via endocytosis.[30,31] Given that endocytosis cannot occur in the cell wall, the passive translocation of nanomaterials likely occurred. Recently, computer simulation modeling proposed that graphene microsheets enter cells through passive membrane penetration.[16,32] GOQD was remarkably better internalized than the larger GONS. Zhang and colleagues also proposed that, compared with large GONS, ultrasmall GONS showed a higher amount of cellular uptake in human cells without a cell wall barrier.[33]

Plasmolysis was the most remarkable phenomenon after nanomaterial exposure. In a previous study, we also showed that GONS induced plasmolysis of wheat cells.[34] However, the molecular mechanisms remain unclear. To address this question, the metabolites were detected using metabolomics strategies, as shown in Figure 8. Biotin is an absolute requirement for the full catabolism of isoleucine.[35] The upregulation of isoleucine reduced the biotin concentration and the irritating effects of hydroxyisovalerate, leading to plasma membrane shrinkage.[36] Therefore, nanomaterial-induced plasmolysis likely reflects an increase in isoleucine, as shown in Figure 8c. The mechanisms underlying the increase in

DOI: 10.1021/acsami.5b05328
ACS Appl. Mater. Interfaces 2015, 7, 18104−18112

starch grains after the exposure of nanomaterials also remained unclear. The number of starch grains increased after salt and nitrogen element stimulation in plants.[37,38] The increase in starch grains might reflect cellular adaptation and alterations in nitrogen metabolism. The number of lysosomes also increased after nanomaterial exposure. The lysosome is considered a targeted organ for GONS localization.[5,39] Furthermore, the results of the present study indicate that small GOQD induced the production of more lysosomes than large GONS. Similar to starch grains, the increase in the number of lysosomes might reflect a pattern of cellular adaptation.

Figure 7 shows that cell division is promoted and then inhibited by nanomaterials. Several reasons for this phenomenon have been proposed. First, nanomaterials permeated the cell wall during internalization, promoting the fracture of the cell wall in parental cells.[40] Second, the internalization of nanomaterials damaged the cell ultrastructure, increased oxidative stress, and disturbed cellular metabolism, as shown in Figures 6−8, respectively. Third, the envelopment−internalization synergistic effects led to the inhibition of cell division in Figure 7d. It has been shown that silica coating greatly suppressed cell division.[41] GOQD triggered a more severe inhibition of cell division than GONS did, implying that nanomaterial internalization more strongly influenced cell division than did nanomaterial envelopment. Cell division requires energy, and branched-chain amino acids (BCAAs) provide an alternative to sugar as a source of energy.[42] However, at high concentrations, GONS and GOQD decreased the levels of aspartic acid, which is a precursor of some BCAAs as well as inosine and purine bases,[43] and this would also explain the inhibition of cell division.

GOQD induced stronger biological effects than GONS, i.e., enhancement of the intracellular ROS levels, SOD activity, and mitochondrial membrane potential loss, and the reduction of chlorophyll a and cell division. Reduction of the chlorophyll a content after nanomaterial exposure has been widely reported, although the relevant mechanisms remain unknown.[44,45] Serine participates in the biosynthesis of purines and pyrimidines and is also the precursor of chlorophyll a.[46] Metabolic analysis showed that the serine levels decreased after GONS and GOQD exposure at high concentrations, which explained the reduction in the chlorophyll a content. Mitochondrial membrane potential loss is a common phenomenon in nanotoxicology,[47,48] and oxidative stress is considered the primary mechanism of nanotoxicology,[49,50] but the molecular pathways have not been examined at the metabolic level. Linolenic acid, a membrane lipid, influences the membrane fluidity, and upregulation of this molecule induced perturbations in the plasma membrane.[51] Linolenic acid was also reported as a source of metabolites, called oxylipins.[52] The signaling function of oxylipins is well established because many studies have demonstrated its influence on the peroxidation of free fatty acid chains.[53] Therefore, GOQD likely increased the mitochondrial membrane potential loss and oxidative stress throughupregulation of the linolenic acid content, as shown in Figure 8c. The above discussion suggests that metabolic analysis is potentially useful in the risk analysis of nanomaterials.

CONCLUSION

Multiple parameters of nanomaterials, such as size, dispersity, shape, surface charges, and chemical composition, influence the biological responses to these materials. Notably, the various physicochemical properties of nanomaterials are interdependent. For example, the size of graphene can affect the charge density, dispersity, and density of active groups, conductivity, hydrophobicity, or hydrophilicity.[20,54,55] To avoid the interference of other factors, the ζ potential, surface chemistry, and free electrons of nanomaterials were investigated, as shown in Figure 2. The differences in these factors are not very obvious compared with the size differences between GONS and GOQD, which are 1−5 μm and 20−50 nm in size, respectively. In the present work, size is proposed as the main reason for the differences in the biological responses to GONS and GOQD. GOQD induced more obvious biological effects than GONS, including cellular uptake, cell division, cell permeability, and oxidative stress. Importantly, this work revealed that amino acid metabolism was sensitive to nanomaterial exposure. These metabolites are associated with the biological effects described above. Furthermore, it is proposed that these metabolites could be used as indicators of the corresponding biological responses to nanomaterials of various sizes.

ASSOCIATED CONTENT

Supporting Information

The Supporting Information is available free of charge on the ACS Publications website at DOI: 10.1021/acsami.5b05328.

Nanomaterial characterization, tables regarding the BG-11 medium, proportions of dead cells, and metabolites, and a figure regarding chlorophyll a (PDF)

AUTHOR INFORMATION

Corresponding Authors

*E-mail: huxiangang@nankai.edu.cn. Phone: +86-022-23507800. Fax: +86-022-66229562.

*E-mail: zhouqx@nankai.edu.cn. Phone: +86-022-23507800. Fax: +86-022-66229562.

Notes

The authors declare no competing financial interest.

ACKNOWLEDGMENTS

This work was financially supported by the Ministry of Education of China as an innovative team project (Grant IRT 13024), the National Natural Science Foundation of China (Grants 31170473, 21037002, 21307061, and 21407085), the Tianjin Natural Science Foundation (Grant 14JCQNJC08900), the Specialized Research Fund for the Doctoral Program of Higher Education of China (Grant 2013003112016), and the Postdoctoral Science Foundation of China (Grant 2014M550138).

REFERENCES

(1) Novoselov, K. S.; Fal'ko, V. I.; Colombo, L.; Gellert, P. R.; Schwab, M. G.; Kim, K. A Roadmap for Graphene. *Nature* **2012**, *490*, 192−200.

(2) Dreyer, D. R.; Park, S.; Bielawski, C. W.; Ruoff, R. S. The Chemistry of Graphene Oxide. *Chem. Soc. Rev.* **2010**, *39*, 228−240.

(3) Dikin, D. A.; Stankovich, S.; Zimney, E. J.; Piner, R. D.; Dommett, G. H. B.; Evmenenko, G.; Nguyen, S. T.; Ruoff, R. S. Preparation and Characterization of Graphene Oxide Paper. *Nature* **2007**, *448*, 457−460.

(4) Koenig, S. P.; Boddeti, N. G.; Dunn, M. L.; Bunch, J. S. Ultrastrong Adhesion of Graphene Membranes. *Nat. Nanotechnol.* **2011**, *6*, 543−546.

(5) Kostarelos, K.; Novoselov, K. S. Exploring The Interface of Graphene and Biology. *Science* **2014**, *344*, 261−263.

DOI: 10.1021/acsami.5b05328
ACS Appl. Mater. Interfaces 2015, 7, 18104−18112

(6) Park, J. H.; Yang, S. H.; Lee, J.; Ko, E. H.; Hong, D.; Choi, I. S. Nanocoating of Single Cells: From Maintenance of Cell Viability to Manipulation of Cellular Activities. *Adv. Mater.* **2014**, *26*, 2001−2010.
(7) Kim, B. J.; Park, T.; Moon, H. C.; Park, S.-Y.; Hong, D.; Ko, E. H.; Kim, J. Y.; Hong, J. W.; Han, S. W.; Kim, Y.-G.; Choi, I. S. Cytoprotective Alginate/Polydopamine Core/Shell Microcapsules in Microbial Encapsulation. *Angew. Chem., Int. Ed.* **2014**, *53*, 14443−14446.
(8) Lee, W. C.; Lim, C. H.; Kenry; Su, C.; Loh, K. P.; Lim, C. T. Cell-Assembled Graphene Biocomposite for Enhanced Chondrogenic Differentiation. *Small* **2015**, *11*, 963−969.
(9) Wahid, M. H.; Eroglu, E.; Chen, X.; Smith, S. M.; Raston, C. L. Functional Multi-Layer Graphene-Algae Hybrid Material Formed Using Vortex Fluidics. *Green Chem.* **2013**, *15*, 650−655.
(10) Yang, S. H.; Lee, T.; Seo, E.; Ko, E. H.; Choi, I. S.; Kim, B.-S. Interfacing Living Yeast Cells with Graphene Oxide Nanosheaths. *Macromol. Biosci.* **2012**, *12*, 61−66.
(11) Dallavalle, M.; Calvaresi, M.; Bottoni, A.; Melle-Franco, M.; Zerbetto, F. Graphene Can Wreak Havoc with Cell Membranes. *ACS Appl. Mater. Interfaces* **2015**, *7*, 4406−4414.
(12) Mu, L.; Gao, Y.; Hu, X. L-Cysteine: A biocompatible, Breathable and Beneficial Coating for Graphene Oxide. *Biomaterials* **2015**, *52*, 301−311.
(13) Kostarelos, K.; Lacerda, L.; Pastorin, G.; Wu, W.; Wieckowski, S.; Luangsivilay, J.; Godefroy, S.; Pantarotto, D.; Briand, J.-P.; Muller, S.; Prato, M.; Bianco, A. Cellular Uptake of Functionalized Carbon Nanotubes Is Independent of Functional Group and Cell Type. *Nat. Nanotechnol.* **2007**, *2*, 108−113.
(14) Hu, W.; Peng, C.; Lv, M.; Li, X.; Zhang, Y.; Chen, N.; Fan, C.; Huang, Q. Protein Corona-Mediated Mitigation of Cytotoxicity of Graphene Oxide. *ACS Nano* **2011**, *5*, 3693−3700.
(15) Akhavan, O.; Ghaderi, E. Toxicity of Graphene and Graphene Oxide Nanowalls Against Bacteria. *ACS Nano* **2010**, *4*, 5731−5736.
(16) Zhang, P.; Ma, Y.; Zhang, Z.; He, X.; Li, Y.; Zhang, J.; Zheng, L.; Zhao, Y. Species-Specific Toxicity of Ceria Nanoparticles to *Lactuca* Plants. *Nanotoxicology* **2015**, *9*, 1−8.
(17) Liao, K.-H.; Lin, Y.-S.; Macosko, C. W.; Haynes, C. L. Cytotoxicity of Graphene Oxide and Graphene in Human Erythrocytes and Skin Fibroblasts. *ACS Appl. Mater. Interfaces* **2011**, *3*, 2607−2615.
(18) Geim, A. K.; Novoselov, K. S. The Rise of Graphene. *Nat. Mater.* **2007**, *6*, 183−191.
(19) Li, D.; Mueller, M. B.; Gilje, S.; Kaner, R. B.; Wallace, G. G. Processable Aaqueous Dispersions of Graphene Nanosheets. *Nat. Nanotechnol.* **2008**, *3*, 101−105.
(20) Hu, X.; Zhou, Q. Health and Ecosystem Risks of Graphene. *Chem. Rev.* **2013**, *113*, 3815−35.
(21) Baker, M. Metabolomics: From Small Molecules to Big Ideas. *Nat. Methods* **2011**, *8*, 117−121.
(22) Rouquie, D.; Heneweer, M.; Botham, J.; Ketelslegers, H.; Markell, L.; Pfister, T.; Steiling, W.; Strauss, V.; Hennes, C. Contribution of New Technologies to Characterization and Prediction of Adverse Effects. *Crit. Rev. Toxicol.* **2015**, *45*, 172−183.
(23) Zenobi, R. Single-Cell Metabolomics: Analytical and Biological Perspectives. *Science* **2013**, *342*, 1243259−1243259.
(24) Heller, D. A.; Baik, S.; Eurell, T. E.; Strano, M. S. Single-Walled Carbon Nanotube Spectroscopy in Live Cells: Towards Long-Term Labels and Optical Sensors. *Adv. Mater.* **2005**, *17*, 2793−2799.
(25) Nel, A. E.; Maedler, L.; Velegol, D.; Xia, T.; Hoek, E. M. V.; Somasundaran, P.; Klaessig, F.; Castranova, V.; Thompson, M. Understanding Biophysicochemical Interactions at The Nano-bio Interface. *Nat. Mater.* **2009**, *8*, 543−557.
(26) Powell, R. J.; Hill, R. T. Mechanism of Algal Aggregation by *Bacillus sp* Strain RP1137. *Appl. Environ. Microbiol.* **2014**, *80*, 4042−4050.
(27) Chen, G. Y.; Pang, D. W. P.; Hwang, S. M.; Tuan, H. Y.; Hu, Y. C. A Graphene-Based Platform for Induced Pluripotent Stem Cells Culture and Differentiation. *Biomaterials* **2012**, *33*, 418−427.
(28) Na, H.-K.; Kim, M.-H.; Lee, J.; Kim, Y.-K.; Jang, H.; Lee, K. E.; Park, H.; Heo, W. D.; Jeon, H.; Choi, I. S.; Lee, Y.; Min, D.-H. Cytoprotective Effects of Graphene Oxide for Mammalian Cells Against Internalization of Exogenous Materials. *Nanoscale* **2013**, *5*, 1669−1677.
(29) Kempaiah, R.; Salgado, S.; Chung, W. L.; Maheshwari, V. Graphene as Membrane for Encapsulation of Yeast Cells: Protective and Electrically Conducting. *Chem. Commun.* **2011**, *47*, 11480−11482.
(30) Talukdar, Y.; Rashkow, J. T.; Lalwani, G.; Kanakia, S.; Sitharaman, B. The Effects of Graphene Nanostructures on Mesenchymal Stem Cells. *Biomaterials* **2014**, *35*, 4863−4877.
(31) Shang, W.; Zhang, X.; Zhang, M.; Fan, Z.; Sun, Y.; Han, M.; Fan, L. The Uptake Mechanism and Biocompatibility of Graphene Quantum Dots with Human Neural Stem Cells. *Nanoscale* **2014**, *6*, 5799−5806.
(32) Li, Y.; Yuan, H.; von dem Bussche, A.; Creighton, M.; Hurt, R. H.; Kane, A. B.; Gao, H. Graphene Microsheets Enter Cells Through Spontaneous Membrane Penetration at Edge Asperities and Corner Sites. *Proc. Natl. Acad. Sci. U. S. A.* **2013**, *110*, 12295−12300.
(33) Zhang, H.; Peng, C.; Yang, J.; Lv, M.; Liu, R.; He, D.; Fan, C.; Huang, Q. Uniform Ultrasmall Graphene Oxide Nanosheets with Low Cytotoxicity and High Cellular Uptake. *ACS Appl. Mater. Interfaces* **2013**, *5*, 1761−1767.
(34) Hu, X.; Zhou, M.; Zhou, Q. Ambient Water and Visible-Light Irradiation Drive Changes in Graphene Morphology, Structure, Surface Chemistry, Aggregation, and Toxicity. *Environ. Sci. Technol.* **2015**, *49*, 3410−3418.
(35) Graulet, B.; Matte, J. J.; Desrochers, A.; Doepel, L.; Palin, M. F.; Girard, C. L. Effects of Dietary Supplements of Folic Acid and Vitamin B-12 on Metabolism of Dairy Cows in Early Lactation. *J. Dairy Sci.* **2007**, *90*, 3442−3455.
(36) Cotter, K.; Capecci, J.; Sennoune, S.; Huss, M.; Maier, M.; Martinez-Zaguilan, R.; Forgac, M. Activity of Plasma Membrane V-ATPases Is Critical for The Invasion of MDA-MB231 Breast Cancer Cells. *J. Biol. Chem.* **2015**, *290*, 3680−3692.
(37) Thitisaksakul, M.; Tananuwong, K.; Shoemaker, C. F.; Chun, A.; Tanadul, O.-u.-M.; Labavitch, J. M.; Beckles, D. M. Effects of Timing and Severity of Salinity Stress on Rice (*Oryza sativa L.*) Yield, Grain Composition, and Starch Functionality. *J. Agric. Food Chem.* **2015**, *63*, 2296−2304.
(38) Singh, N.; Pal, N.; Mahajan, G.; Singh, S.; Shevkani, K. Rice Grain and Starch Properties: Effects of Nitrogen Fertilizer Application. *Carbohydr. Polym.* **2011**, *86*, 219−225.
(39) Zhou, N.; Zhu, S.; Maharjan, S.; Hao, Z.; Song, Y.; Zhao, X.; Jiang, Y.; Yang, B.; Lu, L. Elucidating The Endocytosis, Intracellular Trafficking, and Exocytosis of Carbon Dots in Neural Cells. *RSC Adv.* **2014**, *4*, 62086−62095.
(40) Kodama, Y.; Fujishima, M. Cell Division and Density of Symbiotic *Chlorella variabilis* of The Ciliate *Paramecium Bursaria* Is Controlled by The Host's Nutritional Conditions During Early Infection Process. *Environ. Microbiol.* **2012**, *14*, 2800−2811.
(41) Lee, J.; Choi, J.; Park, J. H.; Kim, M.-H.; Hong, D.; Cho, H.; Yang, S. H.; Choi, I. S. Cytoprotective Silica Coating of Individual Mammalian Cells Through Bioinspired Silicification. *Angew. Chem., Int. Ed.* **2014**, *53*, 8056−8059.
(42) Taylor, N. L.; Heazlewood, J. L.; Day, D. A.; Millar, A. H. Lipoic Acid-Dependent Oxidative Catabolism of Alpha-Keto Acids in Mitochondria Provides Evidence for Branched-Chain Amino Acid Catabolism in *Arabidopsis*. *Plant Physiol.* **2004**, *134*, 838−848.
(43) Azevedo, R. A.; Lancien, M.; Lea, P. J. The Aspartic Cid Metabolic Pathway, An Exciting and Essential Pathway in Plants. *Amino Acids* **2006**, *30*, 143−162.
(44) Besseling, E.; Wang, B.; Lurling, M.; Koelmans, A. A. Nanoplastic Affects Growth of *S. obliquus* and Reproduction of *D. magna*. *Environ. Sci. Technol.* **2014**, *48*, 12336−12343.
(45) Perreault, F.; Samadani, M.; Dewez, D. Effect of Soluble Copper Released from Copper Oxide Nanoparticles Solubilisation on Growth and Photosynthetic Processes of *Lemna gibba L. Nanotoxicology* **2014**, *8*, 374−382.

DOI: 10.1021/acsami.5b05328
ACS Appl. Mater. Interfaces 2015, 7, 18104−18112

(46) Toubiana, D.; Batushansky, A.; Tzfadia, O.; Scossa, F.; Khan, A.; Barak, S.; Zamir, D.; Fernie, A. R.; Nikoloski, Z.; Fait, A. Combined Correlation-Based Network and mQTL Analyses Efficiently Identified Loci for Branched-Chain Amino Acid, Serine to Threonine, and Proline Metabolism in Tomato Seeds. *Plant J.* **2015**, *81*, 121−133.
(47) Hoess, S.; Fritzsche, A.; Meyer, C.; Bosch, J.; Meckenstock, R. U.; Totsche, K. U. Size- and Composition-Dependent Toxicity of Synthetic and Soil-Derived Fe Oxide Colloids for The Nematode *Caenorhabditis elegans*. *Environ. Sci. Technol.* **2015**, *49*, 544−552.
(48) Filippi, C.; Pryde, A.; Cowan, P.; Lee, T.; Hayes, P.; Donaldson, K.; Plevris, J.; Stone, V. Toxicology of ZnO and TiO_2 Nanoparticles on Hepatocytes: Impact on Metabolism and Bioenergetics. *Nanotoxicology* **2015**, *9*, 126−134.
(49) Singh, A. V.; Mehta, K. K.; Worley, K.; Dordick, J. S.; Kane, R. S.; Wan, L. Q. Carbon Nanotube-Induced Loss of Multicellular Chirality on Micropatterned Substrate is Mediated by Oxidative Stress. *ACS Nano* **2014**, *8*, 2196−2205.
(50) Lee, Y.-H.; Cheng, F.-Y.; Chiu, H.-W.; Tsai, J.-C.; Fang, C.-Y.; Chen, C.-W.; Wang, Y.-J. Cytotoxicity, Oxidative Stress, Apoptosis and The Autophagic Effects of Silver Nanoparticles in Mouse Embryonic Fibroblasts. *Biomaterials* **2014**, *35*, 4706−4715.
(51) Arouri, A.; Mouritsen, O. G. Membrane-Perturbing Effect of Fatty Acids and Lysolipids. *Prog. Lipid Res.* **2013**, *52*, 130−140.
(52) Howe, G. A.; Schilmiller, A. L. Oxylipin Metabolism in Response to Stress. *Curr. Opin. Plant Biol.* **2002**, *5*, 230−236.
(53) Farmer, E. E.; Mueller, M. J. ROS-Mediated Lipid Peroxidation and RES Activated Signaling. *Annu. Rev. Plant Biol.* **2013**, *64*, 429−450.
(54) Erickson, K.; Erni, R.; Lee, Z.; Alem, N.; Gannett, W.; Zettl, A. Determination of The Local Chemical Structure of Graphene Oxide and Reduced Graphene Oxide. *Adv. Mater.* **2010**, *22*, 4467−4472.
(55) Kim, J.; Cote, L. J.; Kim, F.; Yuan, W.; Shull, K. R.; Huang, J. Graphene Oxide Sheets at Interfaces. *J. Am. Chem. Soc.* **2010**, *132*, 8180−8186.

DOI: 10.1021/acsami.5b05328
ACS Appl. Mater. Interfaces 2015, 7, 18104−18112